Title

Formation and emission of large furans and oxygenated hydrocarbons from flames

Journal

Proceedings of the National Academy of Sciences of the United States of America, 113(30)

ISSN

0027-8424

Authors

Johansson, K Olof

Dillstrom, Tyler

Monti, Matteo

et al.

Publication Date

2016-07-26

DOI

10.1073/pnas.1604772113

Peer reviewed

Formation and emission of large furans and oxygenated hydrocarbons from flames

K. Olof Johansson[a], Tyler Dillstrom[b], Matteo Monti[c], Farid El Gabaly[d], Matthew F. Campbell[a], Paul E. Schrader[a], Denisia M. Popolan-Vaida[e,f], Nicole K. Richards-Henderson[e], Kevin R. Wilson[e], Angela Violi[b,g,h,i,1], and Hope A. Michelsen[a,1]

[a]Combustion Research Facility, Sandia National Laboratories, Livermore, CA 94550; [b]Department of Mechanical Engineering, University of Michigan, Ann Arbor, MI 48109; [c]Department of Materials Science & Engineering, Stanford University, Stanford, CA 94305; [d]Materials Physics, Sandia National Laboratories, Livermore, CA 94550; [e]Chemical Sciences Division, Lawrence Berkeley National Laboratory, Berkeley, CA 94720; [f]Department of Chemistry, University of California, Berkeley, CA 94720; [g]Department of Chemical Engineering, University of Michigan, Ann Arbor, MI 48109; [h]Department of Macromolecular Science and Engineering, University of Michigan, Ann Arbor, MI 48109; and [i]Biophysics Program, University of Michigan, Ann Arbor, MI 48109

Edited by Barbara J. Finlayson-Pitts, University of California, Irvine, CA, and approved June 7, 2016 (received for review March 22, 2016)

Many oxygenated hydrocarbon species formed during combustion, such as furans, are highly toxic and detrimental to human health and the environment. These species may also increase the hygroscopicity of soot and strongly influence the effects of soot on regional and global climate. However, large furans and associated oxygenated species have not previously been observed in flames, and their formation mechanism and interplay with polycyclic aromatic hydrocarbons (PAHs) are poorly understood. We report on a synergistic computational and experimental effort that elucidates the formation of oxygen-embedded compounds, such as furans and other oxygenated hydrocarbons, during the combustion of hydrocarbon fuels. We used ab initio and probabilistic computational techniques to identify low-barrier reaction mechanisms for the formation of large furans and other oxygenated hydrocarbons. We used vacuum-UV photoionization aerosol mass spectrometry and X-ray photoelectron spectroscopy to confirm these predictions. We show that furans are produced in the high-temperature regions of hydrocarbon flames, where they remarkably survive and become the main functional group of oxygenates that incorporate into incipient soot. In controlled flame studies, we discovered ∼100 oxygenated species previously unaccounted for. We found that large alcohols and enols act as precursors to furans, leading to incorporation of oxygen into the carbon skeletons of PAHs. Our results depart dramatically from the crude chemistry of carbon- and oxygen-containing molecules previously considered in hydrocarbon formation and oxidation models and spearhead the emerging understanding of the oxidation chemistry that is critical, for example, to control emissions of toxic and carcinogenic combustion by-products, which also greatly affect global warming.

furans | oxygenated hydrocarbons | soot | organic carbon | black carbon

Oxygenated hydrocarbons produced during combustion can have a wide range of detrimental effects on human health, air quality, and regional and global climate. Furans, for example, are compounds that contain five-membered rings with four carbon atoms and one oxygen atom. They are frequently observed in the exhaust plumes and nearby environment of combustion sources. Many studies have shown that they are toxic, whether ingested or inhaled, and thus pose a considerable threat to human health (1–4). The simplest of these compounds (i.e., unsubstituted furan, C_4H_4O) is a cyclic, dienic ether with a low molecular weight, high volatility, and high lipophilicity. Studies on rats and mice have shown a dose-dependent increase in hepatocellular adenomas and carcinomas, indicating that furan is carcinogenic (4), and furan is marked as a high-priority substance and a carcinogenic risk by the World Health Organization (5).

Combustion sources of furans include biomass burning (6–9), cigarette and pipe smoke (10, 11), waste incineration (12), electronic waste recycling (13, 14), and volcanic activity (15). The polychlorinated dibenzofurans (PCDFs) are among the most notorious environmental pollutants, and the main source of PCDFs is biomass burning (6–9, 16). Nonchlorinated furans and PCDFs have been shown to be kinetically linked (17, 18). Furans released during combustion are often partitioned into particles and are found in ash from peat (9) and wood (6) burning, in primary organic aerosols from meat cooking (19), and in secondary organic aerosols from hydrocarbon oxidation (20, 21). Wood burning for heating and cooking constitute a major human exposure to airborne particulate PCDFs in some parts of the world (22, 23).

Previous work has suggested that oxygenated species can be attached to surfaces of soot particles of varying maturity emitted from flames and diesel engines, even before atmospheric processing (24–32). Functional groups that have been identified include alcohols/enols, carbonyls, peroxies, and ethers. Oxygen atoms bound to organic species on the particle surface have been shown to greatly affect soot hygroscopicity (28) and the ability of soot particles to adsorb atmospheric water vapor and act as cloud-condensation or ice nuclei. Soot particles emitted from combustors, such as diesel engines, are generally hydrophobic, and enhancements in hygroscopic particle emissions could have substantial indirect climate effects via their influence on cloud formation (33). The effect of soot emissions on cloud-nucleation properties is a major uncertainty in climate predictions (34–36).

Despite the impact of large oxygenated hydrocarbons on combustion chemistry, the environment, and human health, very little is

Significance

Furans and related large oxygenated organic carbon species (OC) are highly toxic pollutants. Their integration into soot particles may greatly enhance soot's hygroscopicity, leading to regional and global climate change. We show that furans are the primary oxygenated functional group on soot formed in hydrocarbon combustion and report a reaction scheme that elucidates the interplay between nonoxygenated and oxygenated hydrocarbons. We expect this reaction pathway to be important in many hydrocarbon oxidation systems spanning geosciences, astrophysics, and energy research. We discovered ∼100 oxygenated species previously unaccounted for in hydrocarbon models. This study advances the understanding of the oxidation chemistry of OC, which is critical to many processes, from controlling emissions of toxic combustion by-products to reducing anthropogenic climate change.

Author contributions: A.V. and H.A.M. designed research; K.O.J., T.D., M.M., F.E.G., M.F.C., P.E.S., D.M.P.-V., N.K.R.-H., K.R.W., A.V., and H.A.M. performed research; K.O.J., T.D., M.M., and F.E.G. analyzed data; and K.O.J., T.D., A.V., and H.A.M. wrote the paper.

The authors declare no conflict of interest.

This article is a PNAS Direct Submission.

Freely available online through the PNAS open access option.

[1]To whom correspondence may be addressed. Email: avioli@umich.edu or hamiche@sandia.gov.

This article contains supporting information online at www.pnas.org/lookup/suppl/doi:10.1073/pnas.1604772113/-/DCSupplemental.

known about their formation mechanisms and emissions. In this paper we present evidence of the formation of oxygenated compounds, including furans, during the combustion of hydrocarbon fuels. Via a synergistic approach that includes ab initio methods and a stochastic model in conjunction with experimental measurements, we identify reaction pathways leading to formation of oxygenated compounds during the combustion of ethylene. We recorded aerosol mass spectra sampled from premixed and diffusion flames, using synchrotron-generated vacuum-UV (VUV) radiation for ionization, for comparison with masses of the predicted chemical compositions. The mass spectra show masses of oxygenated species that agree with the atomic compositions predicted by the simulations. Both experiments and simulations demonstrate that ~50% of the mass peaks observed at some flame heights in the mass range 140–350 u (unified atomic mass units) contain signal from oxygenated species. We also recorded X-ray photoelectron spectroscopy (XPS) spectra of soot samples extracted from these flames for further validation of these mechanisms by comparison with functional groups of the predicted oxygenated species incorporated into particles. The XPS measurements confirm formation of furan precursors, hydroxyl groups, early in the soot-formation process and evolution of furan signatures, ether groups, as the combustion and particles evolve.

The present study represents an important step toward the development of predictive models for the oxidation of hydrocarbons, which will require that the presence and reactivity of these oxygenated compounds are taken into account. Understanding the chemistry related to high-temperature hydrocarbon oxidation may provide a key to controlling emissions of harmful combustion byproducts, such as soot, nonchlorinated furans, and PCDFs, leading to multiple environmental and health benefits.

Results and Discussion

Simulations. We investigated new reaction pathways for the formation and decomposition of oxygenated species using ab initio electronic-structure calculations to elucidate how oxygen becomes incorporated into the carbon framework of organic carbon (OC) species and soot. We found a generic furan-formation route with low reaction barriers involving species that are abundant in hydrocarbon flames, such as acetylene. The reaction pathway is likely to end with a unimolecular ring closure, suggesting that there should be a high fraction of furans present among oxygenated OC formed during combustion. Fig. 1 illustrates the barriers (TS1 and TS2) of the unimolecular furan-ring closure by showing the formation of benzofuran from phenoxy-acetylene. The energy barriers are relatively low compared with the average temperature fluctuations in combustion environments.

Reaction rates for different oxygen chemistry pathways were calculated and incorporated into the Stochastic NAnoParticle Simulator (SNAPS) (37) along with kinetic rates from the literature that accounted for different oxygen-adsorption reactions and ring-closure reactions. SNAPS is a probabilistic code that predicts the formation of different soot-precursor molecules and other OC species in flames based on individual reaction trajectories of initial seed molecules as they evolve in the flame.

A premixed C_2H_4/O_2 flame, in which fuel and oxygen are mixed before ignition, was chosen for the SNAPS simulations. SNAPS yielded six main classes of oxygenated groups: alcohol/enol, peroxy acid/radical, ketene, pyran, noncyclic ether, and furan. Alcohols/enols and peroxy acids and radicals are formed via reactions of hydrocarbons with small oxygen-containing molecules, mainly OH and O_2, and serve as precursors to the other four oxygenated groups. Enols containing 6–14 carbon atoms (Fig. S1) account for ~20% of the oxygenated structures close to the burner, where oxygen-containing radicals are present, demonstrating that large enols are important for the chemistry of oxygenated hydrocarbons, and extending the studies of small enols by Taatjes et al. (38) (*Important Enol Intermediates Predicted by SNAPS*). We found that, in addition to the isomerization reaction, removal of enols may proceed via reactions with flame radicals, particularly H and OH, producing oxyradicals. Production of large enols can proceed through radical attacks on the carbon–carbon double bond of enols, followed by alkyl radical addition.

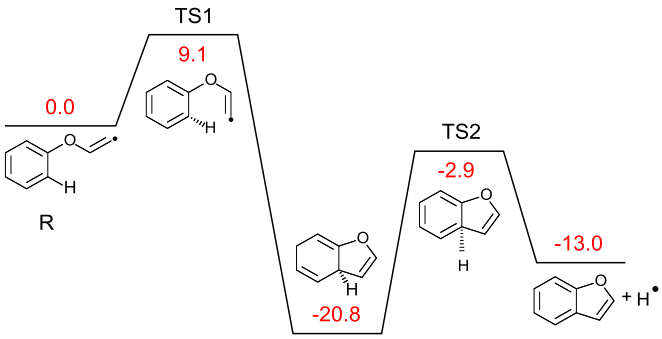

Fig. 1. Potential-energy diagram for the formation of benzofuran. The energies are in kilocalories per mole and are referenced to the reactant species. The ring-closing reaction is exothermic, and the closed-ring structure is thus favored over the open-ring structure. The energy barriers are low compared with the average temperature fluctuations in flames. For example, at 1,500 K, TS1 is $3k_BT$ and TS2 is $-1k_BT$ with respect to the reactant species.

The SNAPS simulations showed that ketenes are formed as the result of oxyradicals present on the terminal carbon of aliphatic chains. Noncyclic ethers are produced when hydrocarbons add to oxyradical sites, following three evolution pathways: (*i*) decomposition, (*ii*) continued hydrocarbon addition, or (*iii*) ring-closure reactions to form furan/pyran groups. Pyran groups are rare, forming when propargyl or methyl and acetylene add to oxyradicals on free-edge sites of aromatic rings, or when acetylene adds to oxyradicals on zigzag sites (see Fig. S2 for site definition). The results also showed potential precursor molecules for formation of dioxins, species with six-membered rings including two oxygen atoms. However, the code does not include any elementary reactions that close a ring containing two oxygen atoms.

Our simulation results demonstrate that oxygen addition to polycyclic aromatic hydrocarbons (PAHs) occurs mainly through consecutive bimolecular reactions resulting in H-abstraction followed by addition of OH or O_2 onto PAH edge sites (*Comments on the SNAPS Modeling*). The most probable pathway for embedding oxygen into the hydrocarbon molecules is via ethers formed when H is abstracted from hydroxyl groups or OH/O is abstracted from peroxy acid/radical groups, followed by hydrocarbon addition to the oxyradical and furan-ring closure. Acetylene is the most frequently added hydrocarbon, and Fig. 2 shows the most probable reaction sequence leading to formation of a furan group. We expect this scheme to be important to a wide range of hydrocarbon oxidation processes and virtually any hydrocarbon-combustion system because of high acetylene concentrations and low reaction barriers. Thus, apart from the toxic potential of furan species, furans may also play a dominant role in determining growth and oxidation sites, radiative forcing potential, and hygroscopic properties of the OC formed during combustion. As these oxygenated OC species evolve in the flame, they can become large enough to condense onto incipient soot particles, leading to incorporation of oxygen onto the surface of soot. Oxygen embedded in the particle surface is expected to contribute to gaseous oxidation products and affect the further growth and oxidation of the particle (17).

Fig. 3 shows some of the most common structures obtained from SNAPS at 160, 168, 194, and 220 u low in the premixed flame. Many of the ether structures formed are furan precursors. Competing reactions to furan-ring closure in the final step in Fig. 2 includes addition of a second hydrocarbon species (Fig. 3 *A* and *B*) or H-addition forming an R–O–CH=CH_2 group (Fig. 3 *D* and *F*) or acetylene removal. The most common oxygenated structure at

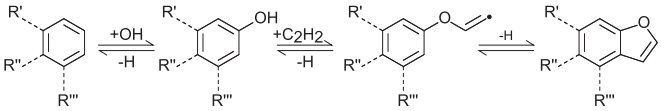

Fig. 2. Most probable reaction sequence leading to formation of a furan group. (*Left* to *Right*) H-abstraction followed by OH addition to the radical free-edge site on an aromatic ring; H-abstraction from the OH group, followed by acetylene addition, forming an ether group; H-elimination during ring closure to form a furan group. The left side of the molecule has been left attached to an indeterminate PAH backbone to illustrate an arbitrary molecular size (see *Comments on the SNAPS Modeling* for details on OH addition).

192 u is the 194-u structure shown in Fig. 3*D* with a furan ring instead of the $–OCHCH_2$ chain; the most common structure at 158 u is the furan formed with the oxygen attached to the phenyl ring in Fig. 3*B* (*Information Related to Fig. 3*). The species in Fig. 3*B* has a ketene group at the terminal carbon of the aliphatic branch, showing that, if acetylene adds to a radical site and OH or O_2 adds to the acetylene chain, a ketene may form instead of a furan and that aliphatic side chains provide sites for the formation of carbonyl bonds.

The evolution of the structure in Fig. 3*F* frequently proceeds via acetylene loss from the oxygen atom or formation of a pyran ring with the zigzag-site carbon, yielding a structure with mass 218 u. Many of the furans formed are potential PCDF precursors (e.g., the substituted dibenzofuran in Fig. 3*E*), although naphtho [2,1-*b*]furan is more common in the simulations than dibenzofuran at 168 u (Fig. 3*C*). The majority of the species predicted by SNAPS experienced molecular growth as they evolved in the flame, and furans constituted the largest group of oxygenated species at large distance from the fuel outlet (DFFO), where the flame temperature was around 1,750 K. An important furan-destruction pathway identified in the simulations is CO reactions: CO can open furan rings and abstract the oxygen atom to form CO_2, leaving the original furan ring as an aliphatic radical side chain. This mechanism may explain the observed aliphatics on the surface of soot particles under some conditions (25, 27, 31, 39).

Aerosol Mass Spectrometry. To support and validate our modeling results, we studied two McKenna-type premixed C_2H_4/O_2 flames with equivalence ratios matching the flame studied using SNAPS and a counterflow diffusion (CF) flame (*Burners and Gas Flows*). In premixed combustion the oxidizer is mixed with the fuel before reaching the flame front, and the concentration of volatile oxygenated hydrocarbons is expected to peak at small DFFOs where OH and O_2 are present. In the CF flame, fuel and oxidizer are fed separately via counterpropagating flows; mixing of fuel and oxidizer takes place across the gas-stagnation plane formed by the counterpropagating flows. The CF flame is an excellent flame for comparison with premixed combustion because there is no oxygen available at small DFFOs, and large oxygenated structures cannot be present at small DFFOs. Hydrocarbon growth initially takes place under pyrolytic conditions, and particles are horizontally convected away from the flame parallel to the gas-stagnation plane, where the vertical velocity component vanishes.

We performed synchrotron-coupled VUV aerosol mass spectrometry (AMS) of soot particles drawn from the different flames and injected directly into the mass spectrometer using an aerodynamic lens system (ADLS) (see *AMS* for more details). Large gas-phase species can condense onto particles in the sampling line between the flame and the ADLS, which leads to physical growth of the particles while the chemistry is frozen, allowing small particles to reach sizes that can be efficiently focused by the ADLS. The particle growth also permits us to detect large gas-phase OC species that are prone to condense onto soot particles at atmospheric temperatures but not at flame temperatures. Species condensed onto soot particles are vaporized in the ionization region of the mass spectrometer without changing species internal composition and mass. Fig. 4 shows example mass spectra of species drawn from three DFFOs in a premixed flame. The results are consistent with the SNAPS simulations and demonstrate that a remarkably large fraction (~50%) of the mass peaks is associated with oxygen inclusion (*Determination of Precise Masses and Atomic Constituents*, Table S1, *Nominal Masses of Oxygen-Containing Species Determined from the Aerosol Mass Spectra*, and Table S2). Mass peaks identified as being associated with oxygenated species are highlighted in red in Fig. 4. The masses of these species (Table S2) agree with the masses of oxygenated OC species predicted by SNAPS, that is, the experimentally observed and predicted species have the same atomic compositions (Table S1). Our AMS studies revealed that these oxygenated species are present under a very wide range of combustion conditions, suggesting generic formation mechanisms.

Fig. 4 shows that the signal from oxygenated OC gets weaker at larger DFFOs in premixed flames, which indicates that they are only formed at low DFFOs in premixed combustion (i.e., where small oxygen-containing species, such as OH and O_2, are present). The SNAPS simulations showed that oxygen addition to PAHs occurred predominantly below a DFFO of 2 mm (Fig. S3), where the concentrations of reactive oxygen (e.g., OH and O_2) are significant in these flames. The soot particles are, however, too small below a DFFO of 3.4 mm to yield signal in the mass spectrometer (see *AMS* for details). Hence, the mass spectrum in Fig. 4*A* was recorded at a DFFO of ~3.5 mm. The SNAPS simulations predicted that the oxygenated species continue to grow as they evolve in the flame, which is consistent with the signal decrease for the red peaks in Fig. 4 with increasing DFFO. As their sizes increase and they become less volatile, they are likely to condense onto incipient soot particles and become integrated into the soot, which further reduces their volatility and prevents them from being vaporized in the ionization region of the AMS instrument. Hence, large oxygenated species are expected to avoid detection at large DFFOs.

Fig. 5*A* shows the ion-signal DFFO dependence for 160, 194, and 220 u for a premixed flame (Fig. 3 displays major predicted structures for these masses). These three masses are indicated by arrows in Fig. 4. Their spatial profiles peak at the lowest DFFO sampled, and we are unable to experimentally establish the

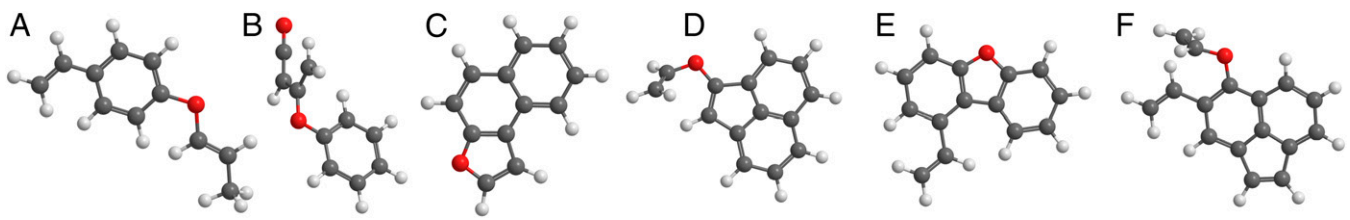

Fig. 3. Frequently predicted oxygen-containing structures of selected masses low in a premixed flame. Red atoms, oxygen; gray, carbon; white, hydrogen. (*A* and *B*) Ether and ether/ketene, 160 u. (*C*) Furan, 168 u. (*D* and *E*) Ether and furan, 194 u. (*F*) Ether, 220 u.

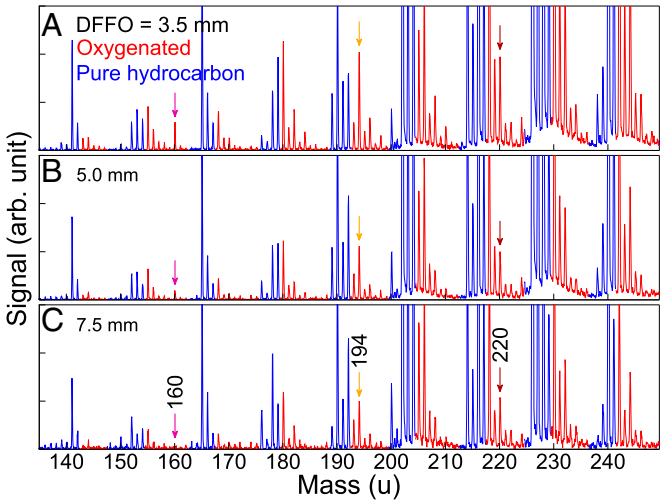

Fig. 4. AMS spectra from a premixed flame. Mass spectra are shown for particles extracted from selected heights in the flame; that is, DFFOs of (*A*) 3.5, (*B*) 5.0, and (*C*) 7.5 mm. Red peaks contain signal from oxygenated species. The arrows indicate the peaks at 160, 194, and 220 u for comparison with Fig. 5*A*; see Fig. 3 for main predicted structures at a DFFO of ∼3.5 mm.

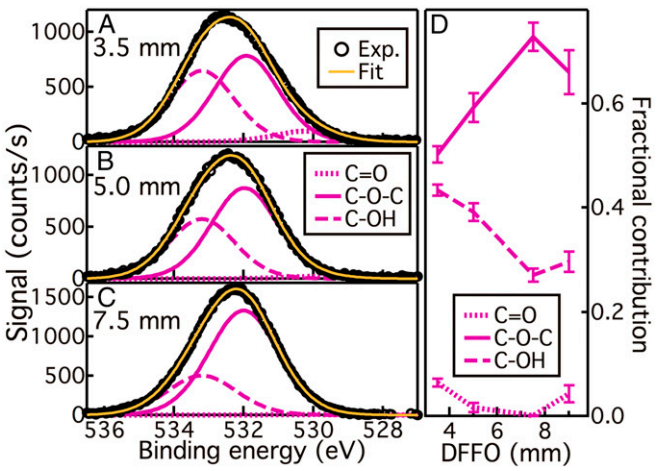

Fig. 6. XPS O 1s spectra of soot sampled from a premixed flame. Spectra are shown for particles extracted from (*A*) a low flame height (DFFO of 3.5 mm), (*B*) an intermediate flame height (DFFO of 5.0 mm), and (*C*) high in the flame (DFFO of 7.5 mm). (*D*) Fractional contributions of oxygenated functional groups were inferred from fits to these and similar XPS O 1s spectra at other DFFOs and plotted as a function of DFFO. Error bars represent ± 1 SD of the uncertainties associated with the peak fits.

location of maximum concentrations because of lack of AMS signal at lower DFFOs. Profiles inferred from mass peaks identified by the SNAPS simulations to stem from pure (nonoxygenated) hydrocarbons, for example $C_{18}H_{10}$ isomers (226 u) and $C_{20}H_{10}$ isomers (250 u), have low intensities at small DFFOs for this flame. Fig. 5*B* shows that the same trend with reactive oxygen was obtained from the CF flame. In the CF flame the growth of hydrocarbon species initially takes place on the fuel side of the flame under pyrolytic conditions, and the reaction scheme in Fig. 2 cannot occur at small DFFOs. We identified many of the same oxygenated masses in the CF flame as in the premixed flames (e.g., 160, 194, and 220 u) (Table S2), and, as expected, they all appear skewed toward the oxygen side of the flame compared with masses identified as pure hydrocarbon masses (e.g., 226 and 250 u), as shown in Fig. 5*B*.

The profiles at 194 and 220 u reach minima at ∼6.5 mm DFFO in Fig. 5*A* and then increase with DFFO. The intensity of the 160-u mass peak does not increase at large DFFOs. Analysis of the exact masses of the 194- and 220-u peaks shows that these two peaks shift slightly toward higher masses with increasing DFFO. These shifts in mass-peak locations indicate that pure hydrocarbons are formed at these two nominal masses at large DFFOs, because the combined mass of one carbon and four hydrogen atoms is slightly larger than the mass of one oxygen atom. These nonoxygenated hydrocarbons increase with increasing DFFO; this observation is consistent with previous gas-phase PAH measurements in sooting premixed flames (e.g., ref. 40). A similar result is obtained in the CF flame (Fig. 5*B*), where the profile at 160 u has a larger shift toward the oxygen side than the profiles at 194 and 220 u, indicating that the signal at 160 u stems entirely from oxygenated species whereas pure hydrocarbon structures contribute to the signals at 194 and 220 u.

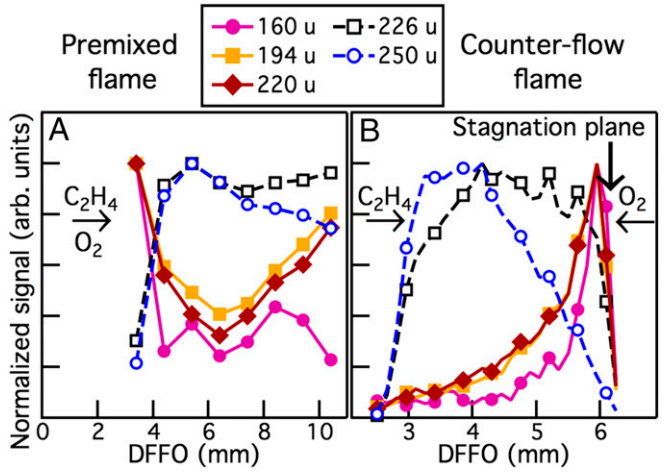

Fig. 5. Normalized signal profiles at selected masses for (*A*) a premixed flame and (*B*) the CF flame. Solid lines refer to masses that include oxygenated species; dashed lines show profiles of nonoxygenated hydrocarbons. For clarity, every third symbol is shown in *B*.

The mass spectra in Fig. 4 are composed of clusters of peaks. The width of each cluster is a crude measure of the spread in hydrogenation among species containing the same number of carbon atoms, because each cluster is largely composed of peaks corresponding to OC species containing a specific number of carbon atoms. The low-mass side of the clusters contain peaks stemming from less-saturated (more aromatic) species without oxygen content. Highly saturated species and species with oxygen atoms appear on the high-mass side of the clusters because an oxygen atom weighs more than the most saturated hydrocarbon group for which it can substitute (i.e., CH_3). The high-mass side of a cluster may also contain signal from species of very low saturation (e.g., odd-carbon-numbered clusters may include signal from the polyyne species containing one additional carbon atom). Hence, on the high-mass side of each cluster are peaks stemming from species that may contain a different number of carbon atoms than the species yielding peaks in the center and on the low-mass side of the cluster. Some oxygenated OC species have nominal masses identical to those of large polyynes and are likely to be misidentified in soot-sample aerosol mass spectra.

XPS. The AMS study confirmed the atomic constituents of the oxygenated OC species predicted by the SNAPS simulations. To validate the predicted OC structures, information on how the oxygen is bonded in the OC molecules is needed. We thus performed XPS studies on soot samples extracted from the premixed flames, as

CHEMISTRY

shown in Fig. 6 (*XPS*). The XPS data verified the SNAPS prediction that alcohol/enol groups are formed low in the flame, and their concentrations decrease with increasing DFFO. The abundance of ethers included in soot particles increases with increasing DFFO, suggesting that alcohols/enols are precursors to ethers. The fractions of C-OH, C-O-C, and C=O species at different DFFOs were determined by analysis of the O 1s spectra (30, 41) and are shown in Fig. 6*D*. The low fraction of C=O species suggests that our soot samples had not been significantly affected by atmospheric oxygen between flame sampling and XPS measurements (42). The strong XPS signal from oxygen-containing functional groups at large DFFOs suggests that the reduced signal from the mass peaks correlated with oxygen inclusion in the mass spectra recorded at DFFOs of 5.0 mm and 7.5 mm (Fig. 4 *B* and *C*) compared with the mass spectrum recorded at a DFFO of 3.5 mm (Fig. 4*A*) is not due to lack of oxygenated OC in the soot. This observation is consistent with incorporation of oxygenated OC in the soot at larger DFFOs, as predicted based on the SNAPS simulations and the AMS studies.

Summary and Conclusions

Despite the distinctly different flame conditions for premixed and diffusion-controlled combustion, we observed consistent masses and behavior regarding formation of oxygenated OC, supporting the generality of large-oxygenate formation, as described in Fig. 2. These reaction pathways are expected to have substantial impact on soot properties, such as hygroscopicity and toxicity. The apparent generality of these chemical mechanisms also suggests that they are important to hydrocarbon oxidation systems other than combustion and may be important in geophysics, astrophysics, and energy research.

We discovered ∼100 oxygenated species previously unaccounted for in hydrocarbon-mass-growth and oxidation models. Under the present configurations, oxygen addition to PAHs occurs mainly via reactions with OH and O_2. Enols and alcohols that result from these reactions act as precursors to ethers, such as furans and pyrans. Furans are produced in the high-temperature regions of hydrocarbon flames, and they remarkably survive and become the main functional group of oxygenates in the OC on soot particles. Cyclic ethers therefore play a more important role than carbonyl and hydroxyl groups during some phases of organic carbon oxidation and may require inclusion in many hydrocarbon oxidation mechanisms and in models aimed at predicting toxicity and hygroscopicity of soot particles and related OC.

The oxygenated OC species discovered in the present study seem to readily become partitioned into incipient soot particles, the lighter ones at atmospheric temperatures and the heavier ones also at flame temperatures. These species should therefore be integral to the molecular-growth pathways leading to soot formation as well as to OC coating of soot particles in the combustor and in the atmosphere. The emission of oxygenated OC and soot can be minimized by an oxygen-rich postcombustion zone at an elevated temperature that should be kept below the threshold for NO_x formation. Furans can be removed through CO reactions as identified by the SNAPS simulations.

Further studies are needed to improve the knowledge of carbon–oxygen interactions in the oxidation and growth chemistry discussed here. Understanding how soot forms and interacts with OC can lead to more efficient combustion technologies that reduce soot emissions, which would have many benefits (e.g., reduced global warming and anthropogenic hydrological impact and reduced concentrations of toxic and carcinogenic environmental pollutants). Flame studies of soot and related OC are, however, also important because they can provide benchmarks for hydrocarbon growth and oxidation models important in other research fields, such as astrophysics (43) and fuel cells (44).

Methods

Computational Approach. Chemical kinetics simulations were performed using SNAPS (37, 45) (*Comments on the SNAPS Modeling*). Briefly, SNAPS is Monte Carlo-based and simulates trajectories of reversible reactions for given seed molecules. General insights into the growth/consumption processes require analysis of a large number of trajectories. SNAPS necessitates information on temperature and gas-phase species concentrations. These inputs were computed by solving the gas-energy equation using the PREMIX program in CHEMKIN (46) with the gas-phase mechanism from Appel et al. (47) because it best represented an average of the speciation profiles generated when using four well-validated gas-phase mechanisms [Appel et al. (47), Miller and Melius (48), Richter et al. (49), and Raj et al. (50)]. Benzene and toluene were used as seed molecules because formation of the first aromatic ring is considered to be the first step in soot formation (51). Molecules formed in the simulations were classified by carbon configuration using social permutation invariant topological coordinates (52); see ref. 37 for more details.

Electronic-structure calculations were carried out using the CBS-QB3 method (53) as implemented in Gaussian 09 (54). Singlet, doublet, and triplet spin multiplicities were tested for the reactant, and the lowest energy (doublet) was determined to be the ground state and thus used for all subsequent calculations. Intrinsic reaction-coordinate calculations were carried out at the B3LYP/CBS level to ensure that each optimized transition state connected the expected reactant and product.

Experimental Approach. Information about the burners and the gas flows are available in *Burners and Gas Flows*. Briefly, the premixed burner is a McKenna design with a 38.1-mm sintered-brass plug surrounded by a shroud-gas sintered-brass ring. The counterflow diffusion burner consists of two vertically mounted, central flow tubes, facing each other, 12 mm apart. They have a 12.7-mm inner diameter and are surrounded by outer flow tubes that help shield the flame from the surroundings. Fuel and oxidizer were fed separately via counterpropagating flows; mixing of fuel and oxidizer took place across the gas-stagnation plane formed by the counterpropagating flows. Hydrocarbon growth initially takes place under pyrolytic conditions, and particles are horizontally convected away from the flame parallel to the gas-stagnation plane, where the vertical velocity component vanishes.

Soot particles were sampled along the vertical centerline of the flames using a quartz probe with a tapered tip. The probe assembly is fixed, and, to sample from different DFFOs, the burner assembly is translated vertically. In the AMS measurements, the sample enters an ADLS (55, 56), which focuses particles larger than ∼50 nm diameter into a beam. Condensation in the sampling line leads to particle growth, which enables some particles that are originally smaller than 50 nm to be focused by the ADLS onto a target heated to ∼570 K inside a vacuum chamber (∼7×10^{-7} Torr). Species that vaporize from the heated target are photoionized using VUV radiation at 9.6 eV, generated at the Advanced Light Source (ALS) synchrotron facility at Lawrence Berkeley National Laboratory. The molecular ions generated are pulse-extracted into a time-of-flight mass spectrometer at a rate of 15 kHz, and mass spectra are recorded using a multichannel scaler. Additional information about the aerosol mass spectrometry investigation is available in *AMS*.

Soot samples for the XPS measurements were collected by extracting particles from the N_2-diluted premixed flame using quartz microprobes from the same batch of probes that was used for the AMS measurements. The particles were drawn from different points along the vertical centerline of the flame at the same flow rate as was used during the AMS studies. The particles were passed through an aerosol neutralizer (TSI 3087) and collected on clean disks of pure aluminum (99.5 pure, 12.5-mm diameter; Goodfellow) using a nanometer aerosol sampler (TSI 3089).

The XPS measurements were performed under ultra-high vacuum conditions (residual pressure $<1 \times 10^{-9}$ Torr) using an Omicron DAR400 Mg K-alpha X-ray source and Physical Electronics 10–360 electron energy analyzer. The spectra shown have not been corrected or processed apart from a background subtraction. The calibration of our instrument was confirmed by measuring a clean sample of highly oriented pyrolytic graphite, which gives a sharp C 1s peak centered at 284.4 eV and FWHM of 1.2 eV, in good agreement with the literature (30, 41). The fitting process, quantitative analysis, and error estimation were performed using the CasaXPS software. All XPS peaks were baseline-corrected using a Shirley background, and a mixed Gaussian–Lorentzian (70%/30%) line shape was used to fit the spectra. The O 1s photoemission spectra were deconvolved using three components corresponding to the oxygen functional groups: C-OH (533.2 eV), C-O-C (531.9 eV), and C=O (530.2 eV), according to Müller et al. (30).

ACKNOWLEDGMENTS. We thank Prof. Barbara Finlayson-Pitts for providing valuable input on an earlier version of our manuscript and to Dr. Paolo Elvati for insightful discussions. This work was funded by the US Department of Energy (DOE) Office of Basic Energy Sciences (BES), Single Investigator Small

Group Research Grant DE-SC0002619 (to A.V., T.D., and K.O.J.), and an Alexander von Humboldt Foundation Feodor Lynen Fellowship (to D.M.P.-V.). Experimental expenses, including burner design and construction, were funded under DOE BES, the Division of Chemical Sciences, Geosciences, and Biosciences (M.F.C., P.E.S., and H.A.M.). Aerosol mass spectrometry measurements were performed at the Advanced Light Source (ALS) at Lawrence Berkeley National Laboratory. The ALS, N.K.R.-H., and K.R.W. were supported by the Director, DOE BES, under Contract DE-AC02-05CH11231. Experimental preparations and XPS measurements were performed at Sandia National Laboratories, which is a multiprogram laboratory managed and operated by Sandia Corporation, a wholly owned subsidiary of Lockheed Martin Company, for the DOE's National Nuclear Security Administration under Contract DE-AC04-94-AL85000.

1. Peterson LA (2006) Electrophilic intermediates produced by bioactivation of furan. *Drug Metab Rev* 38(4):615–626.
2. Ravindranath V, Burka LT, Boyd MR (1984) Reactive metabolites from the bioactivation of toxic methylfurans. *Science* 224(4651):884–886.
3. Monien BH, Herrmann K, Florian S, Glatt H (2011) Metabolic activation of furfuryl alcohol: Formation of 2-methylfuranyl DNA adducts in Salmonella typhimurium strains expressing human sulfotransferase 1A1 and in FVB/N mice. *Carcinogenesis* 32(10):1533–1539.
4. National Institutes of Health (1993) Toxicology and carcinogenesis studies of furan (CAS No. 110-00-9) in F344 rats and B6C3F1 mice (gavage studies). *Natl Toxicol Program Tech Rep Ser* 402:1–286.
5. World Health Organization (2014) IARC monographs on the evaluation of carcinogenic risks to humans, Internal report 14/002 (World Health Organization, Lyon, France).
6. Lavric ED, Konnov AA, De Ruyck J (2004) Dioxin levels in wood combustion—A review. *Biomass Bioenergy* 26(2):115–145.
7. Tame NW, Dlugogorski BZ, Kennedy EM (2007) Formation of dioxins and furans during combustion of treated wood. *Prog Energy Combust Sci* 33(4):384–408.
8. Czuczwa JM, McVeety BD, Hites RA (1984) Polychlorinated dibenzo-p-dioxins and dibenzofurans in sediments from Siskiwit Lake, Isle Royale. *Science* 226(4674):568–569.
9. Meharg AA, Killham K (2003) Environment: A pre-industrial source of dioxins and furans. *Nature* 421(6926):909–910.
10. Sanders EB, Goldsmith AI, Seeman JI (2003) A model that distinguishes the pyrolysis of D-glucose, D-fructose, and sucrose from that of cellulose. Application to the understanding of cigarette smoke formation. *J Anal Appl Pyrolysis* 66(1):29–50.
11. Schubert J, Bewersdorff J, Luch A, Schulz TG (2012) Waterpipe smoke: A considerable source of human exposure against furanic compounds. *Anal Chim Acta* 709:105–112.
12. Valberg PA, Drivas PJ, McCarthy S, Watson AY (1996) Evaluating the health impacts of incinerator emissions. *J Hazard Mater* 47(1):205–227.
13. Man M, Naidu R, Wong MH (2013) Persistent toxic substances released from uncontrolled e-waste recycling and actions for the future. *Sci Total Environ* 463-464:1133–1137.
14. Grant K, et al. (2013) Health consequences of exposure to e-waste: A systematic review. *Lancet Glob Health* 1(6):e350–e361.
15. Tassi F, Montegrossi G, Capecchiacci F, Vaselli O (2010) Origin and distribution of thiophenes and furans in gas discharges from active volcanoes and geothermal systems. *Int J Mol Sci* 11(4):1434–1457.
16. Meharg AA, Osborn D (1995) Dioxins released from chemical accidents. *Nature* 375(6530):353–354.
17. Wilhelm J, Stieglitz L, Dinjus E, Will R (2001) Mechanistic studies on the role of PAHs and related compounds in PCDD/F formation on model fly ashes. *Chemosphere* 42(5-7):797–802.
18. Iino F, Imagawa T, Takeuchi M, Sadakata M (1999) De novo synthesis mechanism of polychlorinated dibenzofurans from polycyclic aromatic hydrocarbons and the characteristic isomers of polychlorinated naphthalenes. *Environ Sci Technol* 33(7):1038–1043.
19. Seinfeld JH, Pandis SN (1998) *Atmospheric Chemistry and Physics: From Air Pollution to Climate Change* (Wiley, New York).
20. Atkinson R, Arey J, Aschmann SM (2008) Atmospheric chemistry of alkanes: Review and recent developments. *Atmos Environ* 42(23):5859–5871.
21. Schilling Fahnestock KA, et al. (2015) Secondary organic aerosol composition from C12 alkanes. *J Phys Chem A* 119(19):4281–4297.
22. Northcross AL, Hammond SK, Canuz E, Smith KR (2012) Dioxin inhalation doses from wood combustion in indoor cookfires. *Atmos Environ* 49:415–418.
23. Pieters R, Focant J-F (2014) Dioxin, furan and PCB serum levels in a South African Tswana population: Comparing the polluting effects of using different cooking and heating fuels. *Environ Int* 66:71–78.
24. Cain J, Laskin A, Kholghy MR, Thomson MJ, Wang H (2014) Molecular characterization of organic content of soot along the centerline of a coflow diffusion flame. *Phys Chem Chem Phys* 16(47):25862–25875.
25. McKinnon JT, Meyer E, Howard JB (1996) Infrared analysis of flame generated PAH samples. *Combust Flame* 105:161–166.
26. Santamaria A, et al. (2006) FT-IR and 1H NMR characterization of the products of an ethylene inverse diffusion flame. *Combust Flame* 146:52–62.
27. di Stasio S, Braun A (2006) Comparative NEXAFS study on soot obtained from an ethylene/air flame, a Diesel engine, and graphite. *Energy Fuels* 20:187–194.
28. Commodo M, Falco GD, Larciprete R, D'Anna A, Minutolo P (2016) On the hydrophilic/hydrophobic character of carbonaceous nanoparticles formed in laminar premixed flames. *Exp Therm Fluid Sci* 73:56–63.
29. Gaddam CK, Vander Wal RL (2013) Physical and chemical characterization of SIDI engine particulates. *Combust Flame* 160:2517–2528.
30. Müller J-O, Su DS, Wild U, Schlögl R (2007) Bulk and surface structural investigations of diesel engine soot and carbon black. *Phys Chem Chem Phys* 9(30):4018–4025.
31. Cain JP, Gassman PL, Wang H, Laskin A (2010) Micro-FTIR study of soot chemical composition-evidence of aliphatic hydrocarbons on nascent soot surfaces. *Phys Chem Chem Phys* 12(20):5206–5218.
32. Mustafi N, Raine RR, James B (2010) Characterization of exhaust particulates from a dual fuel engine by TGA, XPS, and Raman techniques. *Aerosol Sci Technol* 44(11):954–963.
33. Bond TC, et al. (2013) Bounding the role of black carbon in the climate system: A scientific assessment. *J Geophys Res* 118(11):5380–5552.
34. Zhang R, et al. (2008) Variability in morphology, hygroscopicity, and optical properties of soot aerosols during atmospheric processing. *Proc Natl Acad Sci USA* 105(30):10291–10296.
35. Kaufman YJ, Koren I, Remer LA, Rosenfeld D, Rudich Y (2005) The effect of smoke, dust, and pollution aerosol on shallow cloud development over the Atlantic Ocean. *Proc Natl Acad Sci USA* 102(32):11207–11212.
36. Ramanathan V, et al. (2005) Atmospheric brown clouds: Impacts on South Asian climate and hydrological cycle. *Proc Natl Acad Sci USA* 102(15):5326–5333.
37. Lai JY, Elvati P, Violi A (2014) Stochastic atomistic simulation of polycyclic aromatic hydrocarbon growth in combustion. *Phys Chem Chem Phys* 16(17):7969–7979.
38. Taatjes CA, et al. (2005) Enols are common intermediates in hydrocarbon oxidation. *Science* 308(5730):1887–1889.
39. Öktem B, Tolocka MP, Zhao B, Wang H, Johnston MV (2005) Chemical species associated with the early stage of soot growth in a laminar premixed ethylene–oxygen–argon flame. *Combust Flame* 142(4):364–373.
40. Wartel M, Pauwels J-F, Desgroux P, Mercier X (2011) Pyrene measurements in sooting low pressure methane flames by jet-cooled laser-induced fluorescence. *J Phys Chem A* 115(49):14153–14162.
41. McFeely F, et al. (1974) X-ray photoemission studies of diamond, graphite, and glassy carbon valence bands. *Phys Rev B* 9(12):5268–5278.
42. Han C, Liu Y, Ma J, He H (2012) Key role of organic carbon in the sunlight-enhanced atmospheric aging of soot by O_2. *Proc Natl Acad Sci USA* 109(52):21250–21255.
43. Gudipati MS, Yang R (2012) In-situ probing of radiation-induced processing of organics in astrophysical ice analogs—Novel laser desorption laser ionization time-of-flight mass spectroscopic studies. *Astrophys J* 756(1):L24.
44. Park S, Vohs JM, Gorte RJ (2000) Direct oxidation of hydrocarbons in a solid-oxide fuel cell. *Nature* 404(6775):265–267.
45. Johansson K, et al. (2015) Soot precursor formation and limitations of the stabilomer grid. *Proc Combust Inst* 35(2):1819–1826.
46. Kee R, et al. (2006) CHEMKIN Release 4.1 (Reaction Design, San Diego).
47. Appel J, Bockhorn H, Frenklach M (2000) Kinetic modeling of soot formation with detailed chemistry and physics: Laminar premixed flames of C_2 hydrocarbons. *Combust Flame* 121(1):122–136.
48. Miller JA, Melius CF (1992) Kinetic and thermodynamic issues in the formation of aromatic compounds in flames of aliphatic fuels. *Combust Flame* 91(1):21–39.
49. Richter H, Benish TG, Mazyar OA, Green WH, Howard JB (2000) Formation of polycyclic aromatic hydrocarbons and their radicals in a nearly sooting premixed benzene flame. *Proc Combust Inst* 28(2):2609–2618.
50. Raj A, Prada IDC, Amer AA, Chung SH (2012) A reaction mechanism for gasoline surrogate fuels for large polycyclic aromatic hydrocarbons. *Combust Flame* 159(2):500–515.
51. Richter H, Howard JB (2000) Formation of polycyclic aromatic hydrocarbons and their growth to soot: A review of chemical reaction pathways. *Pror Energy Combust Sci* 26:565–608.
52. Pietrucci F, Andreoni W (2011) Graph theory meets ab initio molecular dynamics: Atomic structures and transformations at the nanoscale. *Phys Rev Lett* 107(8):085504.
53. Montgomery JA, Jr, Frisch MJ, Ochterski JW, Petersson GA (1999) A complete basis set model chemistry. VI. Use of density functional geometries and frequencies. *J Chem Phys* 110(6):2822–2827.
54. Frisch MJ, et al. (2009) Gaussian 09, Revision A.02 (Gaussian, Inc., Wallingford, CT).
55. Zhang X, et al. (2004) Numerical characterization of particle beam collimation: Part II integrated aerodynamic-lens–nozzle system. *Aerosol Sci Technol* 38(6):619–638.
56. Headrick JM, Schrader PE, Michelsen HA (2013) Radial-profile and divergence measurements of combustion-generated soot focused by an aerodynamic-lens system. *J Aerosol Sci* 58:158–170.
57. Moshammer K, Lucassen A, Togbé C, Kohse-Höinghaus K, Hansen N (2015) Formation of oxygenated and hydrocarbon intermediates in premixed combustion of 2-methylfuran. *Z Phys Chem* 229(4):507–528.
58. Hansen N, Cool TA, Westmoreland PR, Kohse-Höinghaus K (2009) Recent contributions of flame-sampling molecular-beam mass spectrometry to a fundamental understanding of combustion chemistry. *Pror Energy Combust Sci* 35(2):168–191.
59. Guner V, et al. (2003) A standard set of pericyclic reactions of hydrocarbons for the benchmarking of computational methods: The performance of ab initio, density functional, CASSCF, CASPT2, and CBS-QB3 methods for the prediction of activation barriers, reaction energetics, and transition state geometries. *J Phys Chem A* 107(51):11445–11459.
60. Tokmakov I, Lin M (2002) Kinetics and mechanism of the OH+ C_6H_6 reaction: A detailed analysis with first-principles calculations. *J Phys Chem A* 106(46):11309–11326.
61. Bohn B, Zetzsch C (1999) Gas-phase reaction of the OH–benzene adduct with O_2: Reversibility and secondary formation of HO_2. *Phys Chem Chem Phys* 1(22):5097–5107.
62. Seta T, Nakajima M, Miyoshi A (2006) High-temperature reactions of OH radicals with benzene and toluene. *J Phys Chem A* 110(15):5081–5090.
63. Blanquart G, Pepiot-Desjardins P, Pitsch H (2009) Chemical mechanism for high temperature combustion of engine relevant fuels with emphasis on soot precursors. *Combust Flame* 156(3):588–607.
64. Xu ZF, Lin MC (2006) Ab initio kinetics for the unimolecular reaction C_6H_5OH–> CO + C_5H_6. *J Phys Chem A* 110(4):1672–1677.
65. Audi G, Wapstra A (1995) The 1995 update to the atomic mass evaluation. *Nucl Phys A* 595(4):409–480.